AWARD NUMBER: W81XWH-16-1-0653

TITLE: Early Detection of Clinically Significant Prostate Cancer Using Ultrasonic Acoustic Radiation Force Impulse (ARFI) Imaging

PRINCIPAL INVESTIGATOR: Kathryn R. Nightingale

CONTRACTING ORGANIZATION: Duke University
Durham, NC 27708-0281

REPORT DATE: OCTOBER 2018

TYPE OF REPORT: Annual

PREPARED FOR: U.S. Army Medical Research and Materiel Command
Fort Detrick, Maryland 21702-5012

# REPORT DOCUMENTATION PAGE

*Form Approved*
*OMB No. 0704-0188*



| 1. REPORT DATE | 2. REPORT TYPE | 3. DATES COVERED |
|---|---|---|
| OCTOBER 2018 | Annual | 9/15/2017-9/14/2018 |

**4. TITLE AND SUBTITLE**

Early Detection of Clinically Significant Prostate Cancer Using Ultrasonic

Acoustic Radiation Force Impulse (ARFI) Imaging

**5a. CONTRACT NUMBER**

**5b. GRANT NUMBER**
**W81XWH-16-1-0653**

**5c. PROGRAM ELEMENT NUMBER**

**6. AUTHORS(S)**

Kathryn R. Nightingale, PhD

EMAIL: kathy.nightingale@duke.edu

**5d. PROJECT NUMBER**

**5e. TASK NUMBER**

**5f. WORK UNIT NUMBER**

**7. PERFORMING ORGANIZATION NAME(S) AND ADDRESS(ES)**

Duke University
2200 W. Main St. Suite 710
Durham, NC 27708-4677

**8. PERFORMING ORGANIZATION REPORT NUMBER**

**9. SPONSORING / MONITORING AGENCY NAME(S) AND ADDRESS(ES)**

U.S. Army Medical Research and Materiel Command
Fort Detrick, Maryland 21702-5012

**10. SPONSOR/MONITOR'S ACRONYM(S)**
USAMed Research ACQ Activity

**11. SPONSOR/MONITOR'S REPORT NUMBER(S)**

**12. DISTRIBUTION / AVAILABILITY STATEMENT**

Approved for Public Release; Distribution Unlimited

**13. SUPPLEMENTARY NOTES**

**14. ABSTRACT**

Prostate cancer (PCa) is the second most common cancer in men in the United States, with over 220,000 cases newly diagnosed, and over 27,000 deaths annually. Although diagnosis is currently performed by biopsy under ultrasound guidance, the systematic sampling approach has poor sensitivity due in large part to the low specificity of B-mode ultrasound for PCa. Our overall goal is to develop a 3D ultrasound acoustic radiation force impulse (3D-ARFI) elasticity imaging system that can be used in the clinic for first-time biopsy to facilitate targeting prostate biopsies toward regions that are suspicious for clinically significant PCa due to their elevated stiffness. In the past year, we have finalized our sequencing, data acquisition, and real-time processing and 3D display algorithms. We have analyzed our imaging system in tissue mimicking phantoms, and obtained IRB approval for and initiated imaging in patients with prostate cancer who are expecting radical prostatectomy. We have also developed data analysis tools to be used to assess the system performance in the in vivo studies. The impact of this system, if successful, will be to change the standard of care by enabling detection of the most significant disease present in the prostate upon initial biopsy and diagnosis, facilitating improved treatment decisions and patient outcomes.

**15. SUBJECT TERMS**

Prostate Cancer Imaging, Image guided biopsy, Ultrasound elasticity imaging, ARFI imaging

| 16. SECURITY CLASSIFICATION OF: | | | 17. LIMITATION OF ABSTRACT | 18. NUMBER OF PAGES | 19a. NAME OF RESPONSIBLE PERSON |
|---|---|---|---|---|---|
| a. REPORT | b. ABSTRACT | c. THIS PAGE | | | 19b. TELEPHONE NUMBER *(include area code)* |
| Unclassified | Unclassified | Unclassified | Unclassified | 25 | USAMRMC |

TABLE OF CONTENTS

## 1. INTRODUCTION:

Prostate cancer (PCa) is the second most common cancer in men in the United States, with over 220,000 cases newly diagnosed, and over 27,000 deaths annually. Screening methods are now widely used in the United States and Europe to detect PCa, including digital rectal examination (DRE), and prostate-specific antigen (PSA) analysis. Prostate biopsies are performed to diagnose PCa when suspicion is raised through these screening mechanisms. The clinical standard for performing prostate biopsy is ultrasound-guided, transrectal/transperineal, laterally-directed 18G needle cores, with 10-12 cores systematically sampling different regions of the prostate. Current ultrasonic prostate imaging does not facilitate targeting biopsies to suspicious regions because PCa does not have unique B-mode image characteristics that can delineate diseased from normal structures and benign pathologies. Therefore, the current standard of care has poor sensitivity, mainly because the sampling grid only randomly intersects the pathologic tissues. The purpose of our work is to develop a 3D ultrasound acoustic radiation force impulse (3D-ARFI) elasticity imaging system to facilitate targeting prostate biopsies toward regions that are suspicious for clinically significant cancer. The scope of the work includes three specific aims: 1) To develop and implement a clinic-ready 3D ARFI imaging system on a next-generation scanner with a dedicated ARFI power supply using custom sequences and automated probe rotation/positioning to interrogate the entire prostate gland, including the anterior region, with high resolution and real-time data processing. 2) To integrate ARFI & B-mode data in real-time with 3D Slicer for rapid 3D visualization and image volume interpretation, followed by automated transducer positioning in a user-selected image plane for biopsy targeting of CSD, and to assess system performance in phantoms. 3) To evaluate the performance of the clinic-ready 3D ARFI prostate biopsy guidance system in vivo in humans for targeting clinically significant prostate disease in 15 subjects expecting radical prostatectomy using in vivo MR and whole mount histology as the gold standards.

## 2. KEYWORDS:

Prostate Cancer, Elasticity Imaging, Ultrasound, Prostate biopsy, Image-guided biopsy, Acoustic Radiation Force Impulse (ARFI) imaging, 3D Slicer, 3D scan conversion and visualization, Clinically significant prostate cancer biopsy

## 3. ACCOMPLISHMENTS:

**What were the major goals of the project?**

**Research-Specific Tasks:**

| **Specific Aim 1: Develop 3D ARFI imaging prototype** | **Months** | **% Complete** |
|---|---|---|
| **Major Task 1: 3D ARFI implementation** | | |
| Subtask 1: Develop sequencing tools on new scanner, explore multi-focal-zone configurations for range of prostate sizes | 1-6 | 100% |
| Subtask 2: Zoom-mode ARFI single plane implementation | 6-12 | 100% |
| Subtask 3: Perform acoustic output analysis on final sequences | 14-16 | 100% |
| Subtask 4: Optimizing Feedback System for Rotation Stage | 12-18 | 100% |
| **Specific Aim 2: Integrate ARFI/B-mode imaging with 3D-Slicer/PLUS; perform phantom validation studies** | | |
| **Major Task 2: Integration of ARFI with 3D-Slicer/PLUS** | | |
| Subtask 1: Real-time ARFI Image Generation and 3D Slicer Display | 4-16 | 100% |
| Subtask 2: PLUS Biopsy Guidance Integration | 8-18 | 100% |
| **Major Task 3: Phantom Testing and Validation** | Months | Investigator(s) |
| Subtask 1: Prostate volume and lesion localization validation | 10-18 | 100% |
| Subtask 2: User selection of target location validation | 12-18 | 100% |
| Subtask 3: Perform biopsy guided targeting in phantoms | 14-18 | 100% |
| **Specific Aim 3: Pilot clinical study** | | |
| **Major Task 4: Assess performance of 3D ARFI biopsy system** | | |
| Subtask 1: Finalize protocol and obtain IRB approval | 12-18 | 100% |
| Subtask 2: perform 3D-ARFI imaging in patients expecting radical prostatectomy with pre-operative MR image data available | 18-33 | 30% |
| Subtask 3: analyze data comparing ARFI:SWEI and MR images and visibility and resolution of prostatic capsule; publish results | 33-36 | 5% |

**What was accomplished under these goals?**

We are happy to report that we are on schedule with respect to our target goals. In year 2, we completed the remaining work in specific aims 1 and 2, and initiated data acquisition in the aim 3 pilot clinical study.

We finalized our *in vivo* imaging sequences using our custom designed prototype TRUS transducer, and have initiated the aim 3 pilot study. We implemented data processing approaches that generate B-mode and ARFI image planes in real time as each image plane is acquired. We then integrated our real-time 2D ARFI image generation algorithms with the 3D positioning feedback data to facilitate ARFI 3D volume visualization upon

completion of interrogation of the entire prostate (Figure 1). With the current implementation, the entire acquisition/processing/3D visualization process takes less than 17 minutes.

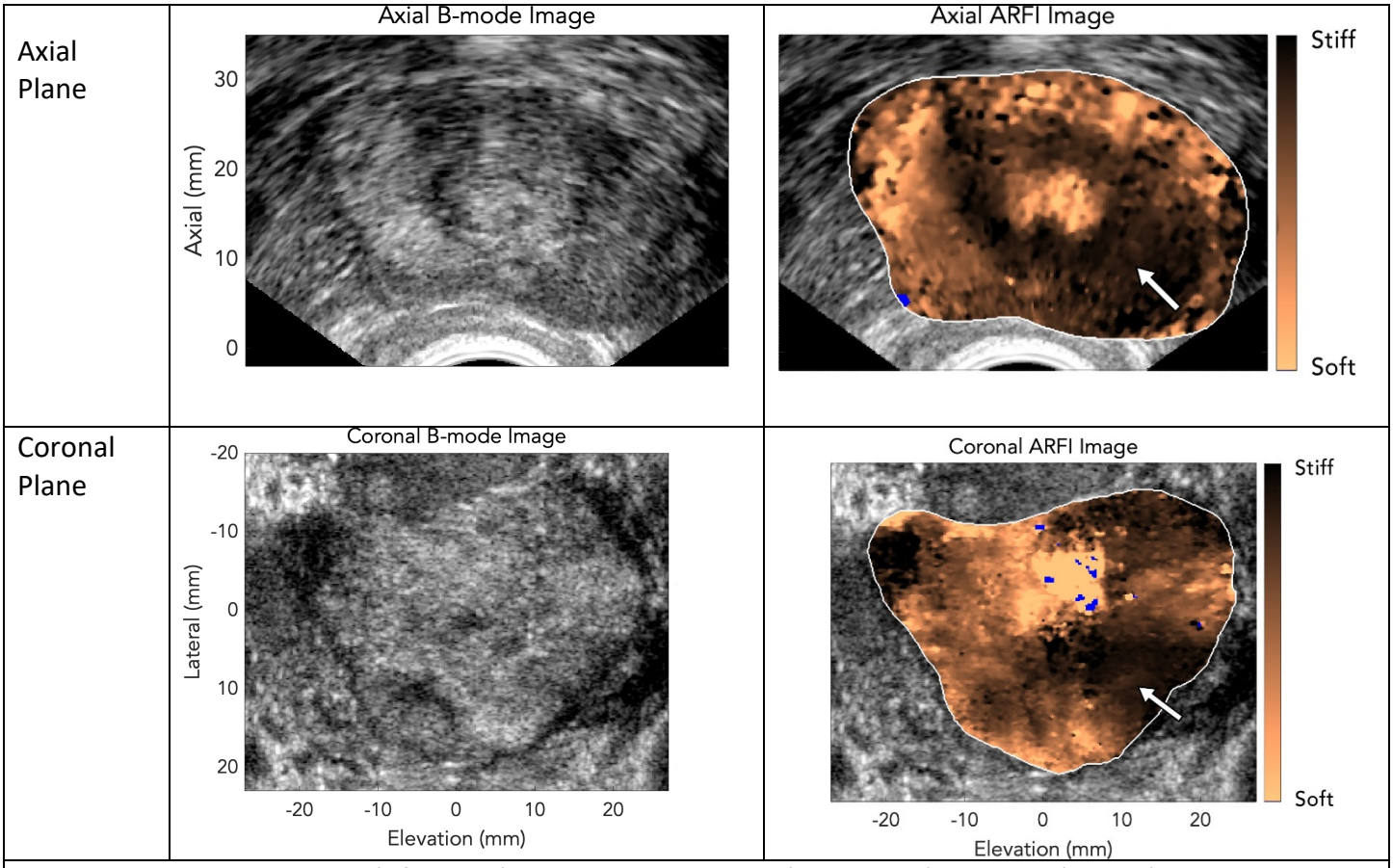


Figure 1: Matched *in vivo* B-mode (left column) and ARFI prostate images (right column) in the axial (top row) and coronal (bottom row) views generated with our 3D ARFI imaging system *in vivo* obtained immediately prior to radical prostatectomy surgery, demonstrating high contrast for a region that was highly suspicious for cancer (white arrow: dark, stiff peripheral zone lesion). Upon excision, this region was determined to be a Gleason 7 prostate cancer in whole-mount histology. The ARFI images have been cropped along the prostate capsule and overlaid on the corresponding B-mode data to provide structural context.

**3D ARFI Imaging Sequence Details:** In the aim 3 clinical imaging studies, ultrasonic data is acquired using a modified Siemens ultrasound scanner (Siemens Medical Solutions, Mountain View, CA) and a custom designed 12L4 side-fire ultrasound probe paired with a custom modified automated rotation stage to acquire sagittal image planes of the prostate. A total of 100 image planes are acquired in each subject spanning the entire gland, with the angular spacing being determined by the overall prostate gland dimensions (ranging anywhere from 0.75 º to 1.5º between image planes). We use a multi-focal zone sequence with optimized parameters given in table 1 for each ARFI excitation. We obtain 16 parallel receive beamlines for each excitation, and monitor the tissue dynamic response to the excitations for 5 msec at a PRF of 5 kHz prior to moving to a new interrogation location within the image plane. We interrogate a total of 68 lateral positions within each sagittal image plane over a 5 cm field of view with 0.74 mm spacing. Data acquisition is triggered by the rotation stage (described below), and, once data acquisition is completed, the rotation stage rotates to the next position.

| Focal Depth (mm) | F/# | Frequency (MHz) | Number of cycles |
|---|---|---|---|

| | | | |
|---|---|---|---|
| Multi-focalzone Push: | | | |
| 15.0 | 2.0 | 4.4 | 300 |
| 22.0 | 2.0 | 4.4 | 300 |
| 30.0 | 2.0 | 4.4 | 300 |
| Track Beams: | | | |
| 60.0 | 2.0 | 4.6 | 1 |

Table 1: Optimal pulse sequences used for the in vivo imaging study in Aim 3.

**Data Processing:** Data is acquired one sagittal image plane at a time, and processing of each image plane occurs during acquisition of subsequent image planes, such that all data processing is completed within 1 minute of the entire volume acquisition. Tissue displacement estimation is performed using the Loupas phase shift estimator with sub-sample interpolation facilitating detection of sub-micron displacements. A correlation coefficient mask with a threshold of 0.95 is applied to the data to limit the impact of noise. Depth dependent gain is applied based upon a phantom reference technique. The real-time ARFI image processing tools directly access raw IQ data in the scanner memory to generate ARFI displacement maps at a user-specified time step after acoustic radiation force excitation. These processing tools have been written in C# to run in a multithreaded CPU infrastructure on the ultrasound scanner, rendering image data in < 1 second/plane. These image data are written to a local disk / memory, where they can be natively read into the 3D Slicer environment for visualization.

**3D Rotation System:**
The rotation setup utilizes a CIVCO Micro-TouchTM stabilizer (CIVCO Medical Solutions, Kalona, IA USA) with 6-axis degrees of freedom for manual positioning of the transducer which has been modified to include automated angular rotation to sweep through the entire prostate during imaging. A custom optical angular feedback transduction circuit utilizing a reflective linear strip with 212 lines-per-inch resolution (US Digital, Vancouver, WA, USA) is coupled to the transducer holding cradle and communicated with a QSB-S Quadrature-to-USB adapter to achieve 9 line / degree resolution. Rotation is performed with a 141 oz-in torque stepper motor with a planetary gearbox (Model #11YPG202S-LW4-R27, Anaheim Automation, 97 Anaheim, CA, USA) to achieve accurate spatial localization of the imaging frames in the 3D dataset (Figure 2). The rotation stage control software is integrated with the ultrasound scanner to provide feedback control for data acquisition, and, the angular positional data is recorded for each image plane that is acquired.

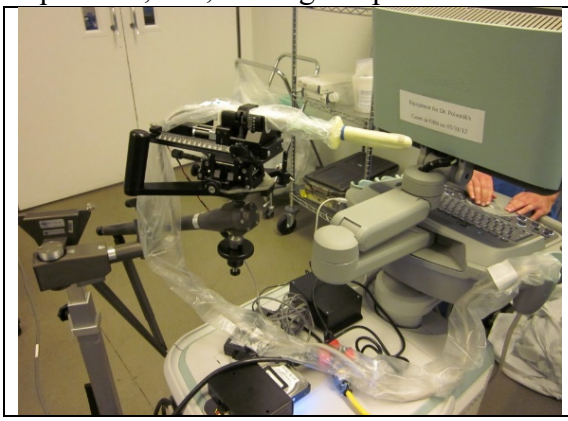

Figure 2: 3D rotation stage setup with CIVCO Micro-TouchTM stabilizer (CIVCO Medical Solutions, Kalona, IA USA) with 6-axis degrees of freedom for manual positioning of the transducer that we have modified to include automated angular rotation to sweep through the entire prostate during imaging.

**3D Visualization:**
Images are scan converted into a 3D volume using 3D Slicer (Kitware Inc., Clifton Park, NY). Each pixel in each image plane is positioned within in a point-cloud using the positional data recorded from the optical positioning system, and scan conversion is performed including outlier removal. Image are read in to the slicer environment via a custom Python module (https://github.com/mlp6/SlicerITKUltrasound). This module can leverage both VTK and ITK (https://github.com/KitwareMedical/ITKUltrasound) 3D interpolation libraries to render 3D ARFI image volumes in 0.2-5 seconds, dependent on the spatial resolution and order of the spatial interpolant.

**Offline SWEI Processing:**
While high resolution ARFI and B-mode image data volumes are generated during data acquisition as shown in Figure 1, we have also developed quantitative shear wave (SWEI) speed estimation techniques that can be applied to the same data. Example matched ARFI and SWEI image planes are shown in Figure 3. Sequence optimization for SWEI data involved assessing the impact of excitation beam spacing on SWEI image SNR. Because the attenuation of shear waves is quite high in prostate tissues, multiple ARFI interrogations are required to obtain sufficient image quality across the entire gland. There is a tradeoff between high density push beam spacing and frame-rate and tissue heating. Figure 4 demonstrates the impact of beam spacing on image SNR for two different transmit voltages. To date we have been processing SWEI data offline due to the larger computational load of this processing approach. The velocity waveform data is first low pass filtered with a cutoff frequency of 1.5 kHz. Then the data is 3D directionally filtered to remove reflection artifacts. Shear wave speeds are estimated using 2D vector tracking, discarding speed estimates greater than 12m/s or with correlation coefficients< 0.6. This work was presented at the 2018 IEEE IUS conference. We are also actively developing multi-parametric image classifiers exploring the utility of combining ARFI and SWEI image data as described below.

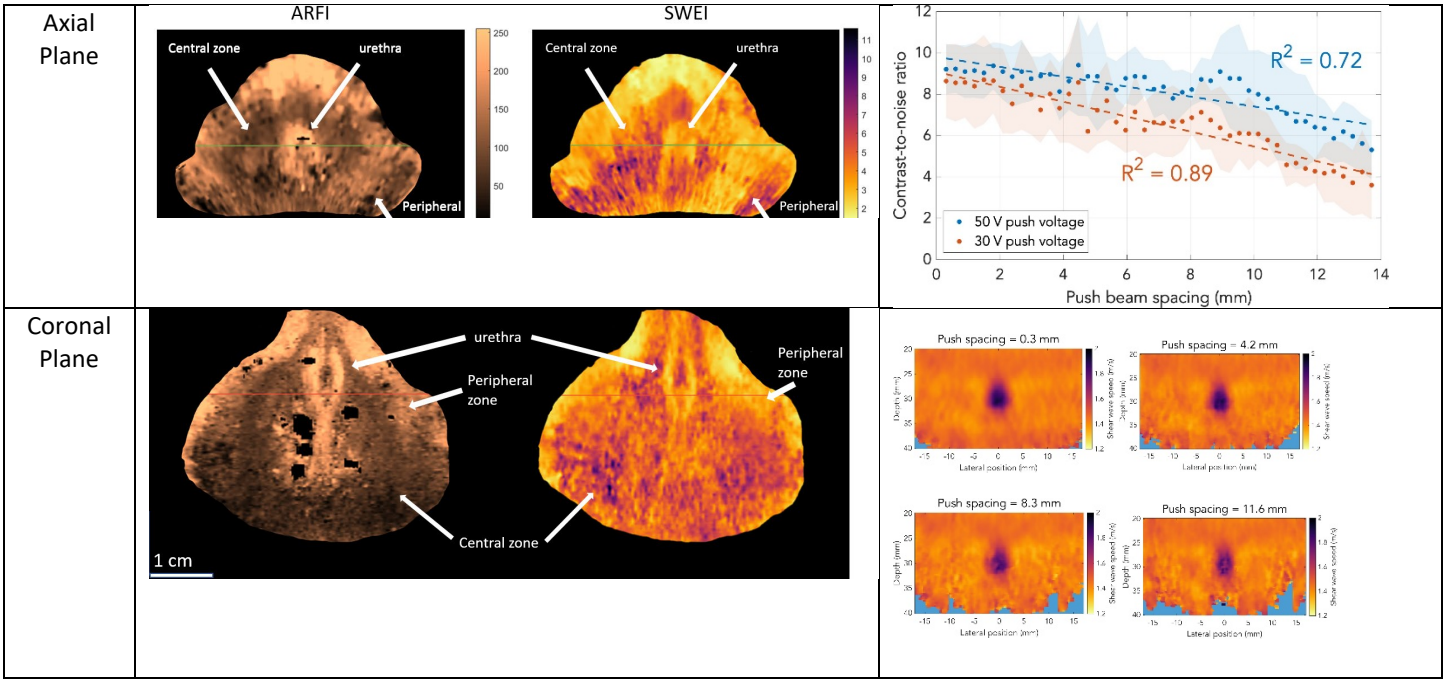

| | |
|---|---|
| Figure 3: Sample *in vivo* ARFI (left) and SWEI (right) images demonstrating structural concordance of normal anatomy in both axial (top row) and coronal (bottom row) imaging planes extracted from 3D image volume datasets obtained during 3D ARFI imaging. | Figure 4: TOP: Push beam spacing vs. contrast-to-noise ratio in phantom lesion images. Bottom: SWEI phantom lesion images for downsampled push beam data. Blue pixels indicate that the speed could not be estimated due to decorrelation. Note that the narrowest spacing has the best CNR and penetration depth. |

**Combined ARFI/SWEI image formation:**

Shear wave elasticity imaging (SWEI) image quality is often degraded by spurious estimates outside the depth of field of the push beam, or by poor spatial resolution due to the reconstruction kernel size. Acoustic radiation force impulse (ARFI) imaging, which tracks displacement within the push beam, typically has greater resolution and depth penetration than SWEI, though it measures only relative stiffness. We have developed a novel framework for enhancing the quality of shear wave elasticity images by combining simultaneously-obtained ARFI and SWEI data using Bayes' theorem, for which the prior distribution is based on local ARFI stiffness information. A likelihood function was formulated for shear wave arrival time estimation based on cross-correlation of particle velocity signals. The prior distribution for the arrival time was constructed using expected relations between shear wave speed, shear modulus, and ARFI displacement magnitude. We evaluated the proposed Bayesian estimator in a calibrated phantom and *in vivo* human prostate data. The range of reconstructed depths was quantified as the range over which the median estimated speed across depth remained within 5% of the quoted speed. As shown in Figure X, the Bayesian estimator increased the range of reconstructed depths by 54.7% (11.6 mm) compared to conventional SWEI. Compared to the on-axis-only reconstruction, the Bayesian estimator resulted in lower bias in the reconstructed speeds (–1.14% vs. –9.14% in the lesion and –1.41% vs. 3.61% in the background) and higher contrast-to-noise ratio (4.95 vs. 1.76). For in vivo prostate data, the Bayesian estimator improved reconstruction image quality, enabling better visualization of the central zone of the prostate (arrow).

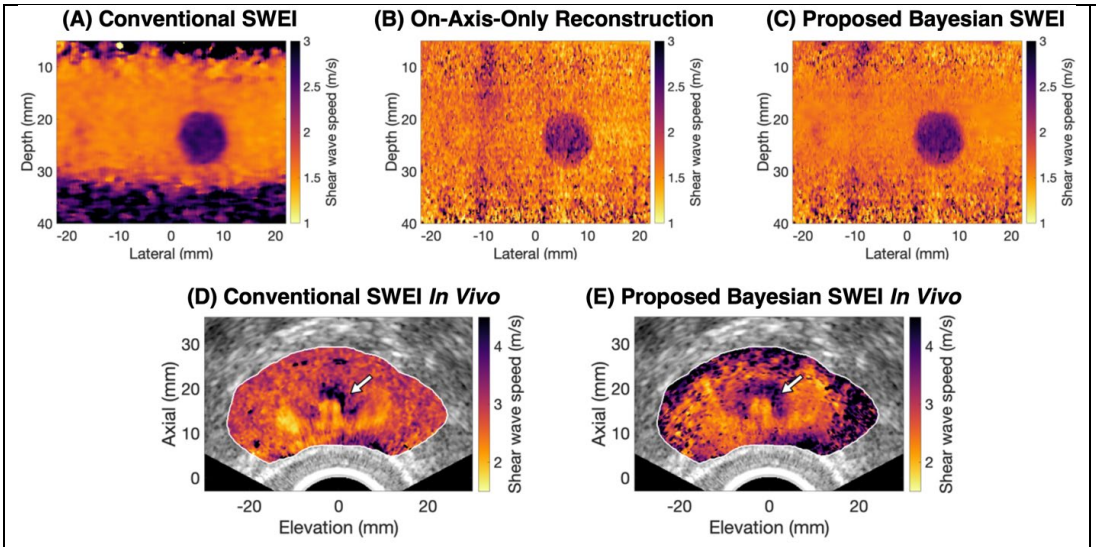


Figure 5: Top row: phantom SWEI images: conventional processing (A); reconstructed image using only the prior (B); Bayes phantom image (C). Bottom row: *In vivo* prostate images with Bayesian method demonstrating improved visualization of the central zone of the prostate (arrow)

**MR:ARFI Data Comparisons:** In year 2 we also developed data analysis tools to compare MR and ARFI imaging data. Figure 5 portrays matched orthogonal axial and coronal image planes from 3D datasets from MR-ADC and ultrasonic elasticity image volumes (ARFI and co-acquired shear wave (SWEI) image volumes) obtained *in vivo* with the corresponding whole-mount histology (post-excision) demonstrating our newly developed data analysis approach. These images demonstrate concordant information across modalities, and, portray the cancer as clearly suspicious in each modality in a common spatial position which would be targeted during ultrasound biopsy (yellow segmentation). To date, we have analyzed previously acquired data with these analysis tools; in the final year of funding we plan to use these tools to evaluate data obtained in the proposed task 4 in vivo studies using our custom designed transducer and custom sequences.

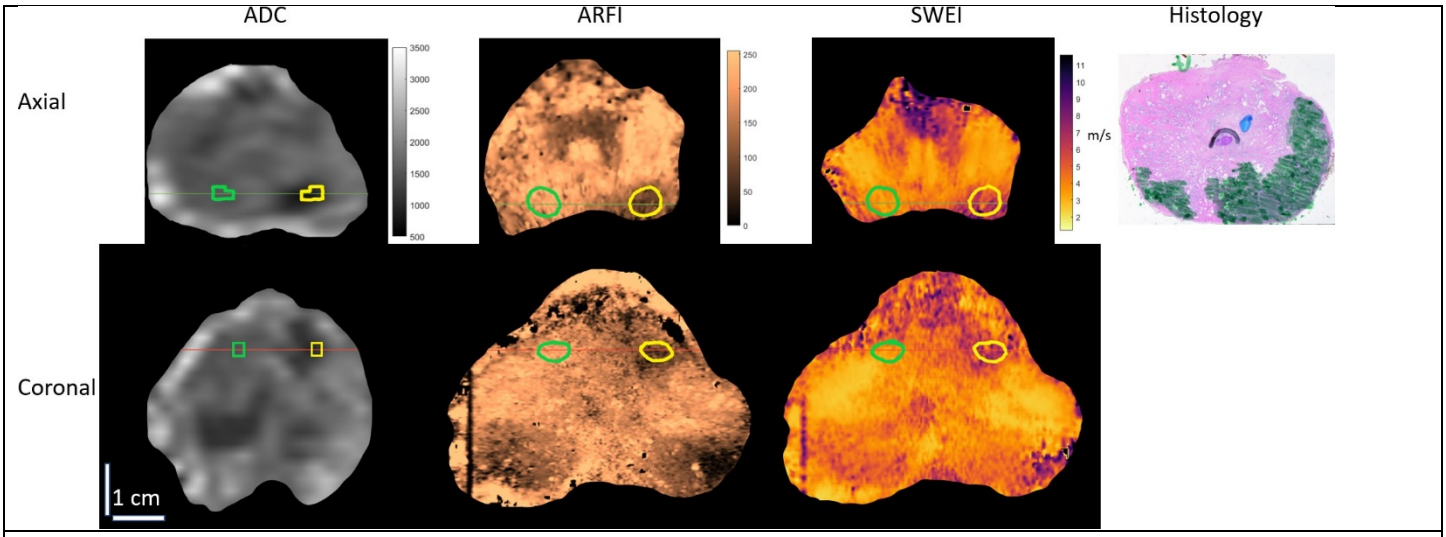


Figure 5: Sample matched mpMRI ADC (left), ARFI (middle-left), SWEI (middle-right), and histology (right) images demonstrating concordance between suspicious targets (yellow outlines) between datasets. These yellow outlined regions would be the targeted location for a biopsy. ARFI and SWEI images are co-acquired and thus perfectly registered while cognitive registration was performed on ADC and histology (Gleason 3 cancerous region colored in green in histology slide). Images from in vivo MR and ARFI/SWEI imaging are shown in two orthogonal views from the 3D image volumes: axial (top) and coronal (bottom). The concordance with MR-ADC and histology demonstrates success in the targeting approach for this example case. The green outlines in the in vivo images are used to define 'healthy' tissue which we require to develop our automated targeting algorithms.

**Classifier Development:** We have initiated studies to compare and explore combining image data from ARFI, SWEI, and MR-ADC (apparent diffusion coefficient) image volumes through classification methods to validate and improve target lesion identification for biopsy targeting. We observe good concordance between MR, ARFI, and SWEI images, as shown in Figure 5. We use post-radical prostatectomy whole mount histology to identify regions of cancerous and healthy tissues from in vivo datasets and manually segment the image volumes via cognitive fusion to develop classifiers for automated identification of biopsy targets. Figure 6 portrays the distribution of values within each patient segmentation completed to date for MRI-ADC (A), ARFI (B), SWEI (C), and the combination of ARFI and SWEI (D).

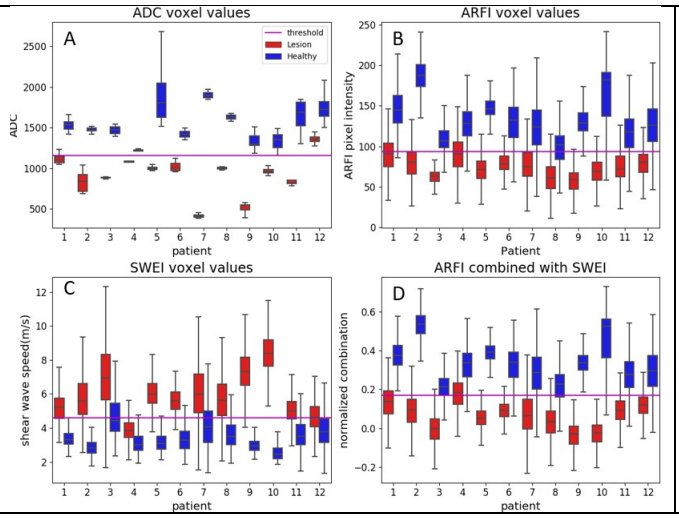


Fig. 6. Images volumes were manually segmented based upon cognitive fusion using histology data to identify healthy and cancerous regions (green and yellow segmentations in Figure 5, respectively). The distribution of values within each patient segmentation completed to date for MRI-ADC (A), ARFI (B), SWEI (C), and the combination of ARFI and SWEI (D). Thresholds are included which are defined by ROC analysis of the entire distribution demonstrating separation of cancerous from healthy image data voxel values in each modality.

Finally, in year 2, we obtained IRB approval for our proposed in vivo studies (subtask 1 of major task 4), and we have initiated data accrual using our custom designed transducer and imaging sequences. During these studies, we process and display the 3D arfi image volumes in the surgical suite using the tools developed under major tasks 1-3 as described above. To date, we have imaged 15 subjects with our optimized system and are on schedule to complete our proposed year 3 efforts.

**What opportunities for training and professional development has the project provided?**

Nothing to report.

**How were the results disseminated to communities of interest?**

Nothing to report.

**What do you plan to do during the next reporting period to accomplish the goals?**

We will complete the remaining tasks in the proposal: the in vivo data acquisition and analysis as proposed in subtasks 2 and 3 of major task 4. We also plan to continue to iterate on our processing algorithms and data analysis approaches to work towards development of an automated targeting algorithm, in addition to exploring the potential benefits of combining image data from multiple modalities (ultrasound, ARFI, SWEI, and MR-ADC) to delineate criteria for prostate cancer detection and staging in ARFI and SWEI image volumes.

## 4. IMPACT:

**What was the impact on the development of the principal discipline(s) of the project?**

We propose to design and build a 3D ARFI ultrasound clinic-ready prostate biopsy guidance system that will enable screening the entire prostate volume for regions suspicious for clinically significant prostate disease (CSD), followed by real-time ultrasonic guidance during first-time targeted needle biopsy of these regions. If, as we hypothesize, this system has the same or better yield for positive biopsy cores for CSD as that obtained with MR-US fusion based targeted prostate biopsy methods, this system has the potential to change the standard of care for prostate cancer diagnosis by enabling detection of the most significant disease present in the prostate upon initial diagnosis, facilitating improved treatment decisions and patient outcomes. Because the proposed system is ultrasonically based, it can be readily integrated with commercial ultrasound scanners, which will enable rapid translation and integration into the current clinical work flow. The additional time required to identify regions suspicious for cancer in the prostate, which could approximately double what is currently required for systematic sampling (30 minutes vs. 15 minutes), will be well warranted given the anticipated improvement in diagnostic outcomes. The ability to make initial treatment decisions based upon first-time biopsy results from the most significant disease present in the gland would lead to a much needed paradigm shift in prostate cancer diagnosis and treatment, significantly reducing the over-treatment and under-diagnosis problems that plague current practice.

**What was the impact on other disciplines?**

The 3D visualization tools that we have developed using the 3D Slicer toolset can be utilized for any image fusion technologies that employ ultrasound.

**What was the impact on technology transfer?**

Nothing to report.

Ultimately, successful completion of this project will pave the way for improving the quality of life for men with suspicion of prostate cancer, as it provides a first step toward enabling accurate diagnosis of the most significant cancer present in the gland upon first-time biopsy, facilitating appropriate treatment decisions.

## 5. CHANGES/PROBLEMS:

Nothing to report.

**Actual or anticipated problems or delays and actions or plans to resolve them**

Nothing to report.

**Changes that had a significant impact on expenditures**

Nothing to report.

**Significant changes in use or care of human subjects, vertebrate animals, biohazards, and/or select agents**

**Significant changes in use or care of human subjects**

Nothing to report.

**Significant changes in use or care of vertebrate animals.**

Not Applicable.

**Significant changes in use of biohazards and/or select agents**

Not Applicable.

6. **PRODUCTS:** List any products resulting from the project during the reporting period. If there is nothing to report under a particular item, state "Nothing to Report."

**Publications, conference papers, and presentations**

**Journal publications**

Nothing to report.

**Books or other non-periodical, one-time publications.**

Nothing to report.

**Other publications, conference papers, and presentations**.

**Presentations:**

Huber M., Morris D., Palmeri M., Nightingale K. "Improving Ultrasound Transducer Control and Tumor Targeting for 3-D Acoustic Radiation Force Impulse Imaging Guided Prostate Biopsy" American Physics Society March Conference, 2018.

Chan D., Lipman S., Rouze N., Morris D., Polascik T., Palmeri M., Nightingale K. "Improving shear-wave speed image quality in 3D prostate elasticity imaging", 43rd International Symposium on Ultrasonic Imaging and Tissue Characterization, June, 2018

**Presentations with Conference Proceedings – presented at IEEE IUS 2018, October 25:**

Chan D., Lipman S., Palmeri M., Morris D., Polascik T., Rouze N., Nightingale K. "Prostate shearwave elastography: multiresolution reconstruction dependence on push beam spacing", *2018 IEEE Ultrasonics Symposium*, Kobe, 2018 (student paper finalist)

Morris D., Chan D., Palmeri M., Glass T., McCormick M., Tay K., Polascik T., Gupta R., Nightingale K. "Correlation between 3D ARFI and quantitative imaging metrics from SWEI and multi-parametric MRI in vivo in normal and cancerous prostate tissue", *2018 IEEE Ultrasonics Symposium*, Kobe, 2018

**Website(s) or other Internet site(s)**

Nothing to report.

**Technologies or techniques**

*Identify technologies or techniques that resulted from the research activities. In addition to a description of the technologies or techniques, describe how they will be shared.*

Nothing to report.

**Inventions, patent applications, and/or licenses**

Nothing to report.

**Other Products**

Nothing to report.

## 7. PARTICIPANTS & OTHER COLLABORATING ORGANIZATIONS-Amberly completing

**What individuals have worked on the project?**

Personnel
Name: **Kathryn Nightingale, Ph.D.**
Project Roll: PI
Nearest person month worked: 1.17 academic months; .5 summer month
Contribution to Project: Dr. Nightingale directs all aspects of the proposed work. She advises the graduate student as he implements the required system sequencing and real-time processing algorithms; coordinates communication between team members during all project phases; interfaces with Siemens during tool development and implementation on the prototype scanner; and oversees the pilot clinical study.
Funding Support: This award

Name: **Mark Palmeri, M.D., Ph.D**.
Project Roll: Co-Investigator
Nearest person month worked: 1.25 summer months
Contribution to Project: Dr. Palmeri oversees and contributes to the real-time implementation of 3D volume rendering and helps to analyze the data from the pilot clinical studies.
Funding Support: This award

Name: **Thomas Polascik, M.D**
Project Roll: Co-Investigator
Nearest person month worked: 0.48 summer months
Contribution to Project: Dr. Polascik is a Professor in the Department of Urology in the Duke University Medical Center. He performs the proposed in vivo ARFI imaging, as well as providing feedback on the 3D visualizations.
Funding Support: This award

Name: **Eileen R. Lanham**
Project Roll: Clinical Research Coordinator
Nearest person month worked: 0.48 calendar months
Contribution to Project: Ms. Lanham performs patient consenting for the project.
Funding Support: This award

Name: **Zoe Charalambous**
Project Roll: Clinical Research Coordinator
Nearest person month worked: 0.12 calendar months
Contribution to Project: Ms. Charalambous performed patient consenting for the project.
Funding Support: This award

Name: **Derek Chan**
Project Roll: Graduate Research Assistant
Nearest person month worked: 12 calendar months
Contribution to Project: Derek is responsible for implementing the technical aspects of the proposed studies, including data processing, algorithm development, and data acquisition in the human and phantom studies.
Funding Support: This award

Name: **Ned Rouze**
Project Roll: Laboratory Manager
Nearest person month worked: 3.12 calendar months
Contribution to Project: Ned oversees the acoustic output measurement studies and thermal studies to ensure patient safety during imaging. He also guides the rotation stage development and implementation.
Funding Support: This award

Name: **Ned Danieley**
Project Roll: Systems Programmer
Nearest person month worked: 2.04
Contribution to Project: Ned manages the storage and HIPAA compliance of the clinical data
Funding Support: This award

**Has there been a change in the active other support of the PD/PI(s) or senior/key personnel since the last reporting period?**

**The following grants have ended since the last progress report**:
**Title:** Ultrasonic Skin Elasticity Measurement Device
**Effort:** 0.25 academic / 1.25 summer (Palmeri)
**Sponsor:** MicroElastic Ultrasound Systems, Inc. /NIH
**Period Funding:** 9/1/17-8/31/18
**Level funding:**
**Goals/Aims:** The constructed device will be validated in a multi-user study using tissue-mimicking phantoms. If successful, Phase II will test the device in patient's post-HCT to see if the device is sensitive and specific enough to detect the onset of GVHD or the response to therapy in way that could meaningfully impact administration of immunosuppression.

**The following new grants have been funded since the last progress report:**
**Title:** A Patient-Adaptive, High MI Abdominal
**Effort**: 1.7 Academic (Nightingale)
1 Academic; 1 Summer (Trahey)
**Sponsor**: NIH 1R01EB026574 (Trahey-PI)
**Grants Management Specialist**: Kwesi Wright

**Period of Performance**: 7/1/18-6/30/23
**Level of funding**:
**Goals**: We propose to construct and clinically evaluate an adaptive ultrasonic scanner that quickly and automatically adjusts system controls to optimize image quality and assists the sonographer in selecting a favorable acoustic window.
**Aims**: 1. To construct an adaptive ultrasonic scanner capable of rapidly and automatically determining and implementing patient-specific imaging parameters based on spatial coherence image quality metrics. 2. With phantom experiments and a pilot clinical study, to further develop spatial and temporal coherence based image quality metrics as feedback parameters used to adaptively select optimal scanner transmit voltage, frequency, focal range(s), and other imaging parameters. 3. To evaluate the clinical impact of patient-adaptive imaging parameter selection, with an option for high MI imaging, on image quality in the HCC screening clinic. To separately evaluate the correlation between image quality and LOC across varying acoustic windows.

**What other organizations were involved as partners?**

Nothing to report.

## 8. SPECIAL REPORTING REQUIREMENTS

Nothing to report.

**9. APPENDICES:** Attach all appendices that contain information that supplements, clarifies or supports the text. Examples include original copies of journal articles, reprints of manuscripts and abstracts, a curriculum vitae, patent applications, study questionnaires, and surveys, etc.

The following IEEE IUS 2018 conference proceedings papers that reported our findings are included in the appendices:

Chan D., Lipman S., Palmeri M., Morris D., Polascik T., Rouze N., Nightingale K. "Prostate shearwave elastography: multiresolution reconstruction dependence on push beam spacing", *2018 IEEE Ultrasonics Symposium*, Kobe, 2018 (student paper finalist)

Morris D., Chan D., Palmeri M., Glass T., McCormick M., Tay K., Polascik T., Gupta R., Nightingale K. "Correlation between 3D ARFI and quantitative imaging metrics from SWEI and multi-parametric MRI in vivo in normal and cancerous prostate tissue", *2018 IEEE Ultrasonics Symposium*, Kobe, 2018

# Prostate Shear Wave Elastography: Multiresolution Reconstruction Dependence on Push Beam Spacing

Derek Y. Chan*, Samantha L. Lipman*, Mark L. Palmeri*, D. Cody Morris*, Thomas J. Polascik†, Ned C. Rouze*, and Kathryn R. Nightingale*
*Department of Biomedical Engineering, Duke University, Durham, NC, USA
†Department of Surgery, Duke University Medical Center, Durham, NC, USA
Email: derek.chan@duke.edu

***Abstract*—This study demonstrates the implementation of a multiresolution shear wave tracking algorithm that enables elasticity imaging of prostate cancer and zonal anatomy. The combined ARFI/SWEI sequence uses closely-spaced push beams across the lateral field of view, with on-axis and off-axis data simultaneously acquired after each push. The shear wave arrival times were determined with cross-correlation of velocity signals in two dimensions after 3-D directional filtering. To combine data from serially interrogated lateral push locations, arrival times from different pushes were aligned by estimating the propagation time between push locations. Shear wave data acquired in an elasticity lesion phantom and reconstructed using this algorithm demonstrate benefits to target contrast-to-noise ratio with increased push beam density and 3-D directional filtering. In human *in vivo* data, histologically-confirmed prostate cancer appears stiff in both SWEI and ARFI images, and regions of the prostate, including the peripheral zone, central gland, and urethra, are visualized.**

## I. Introduction

Prostate cancer is the most common cancer and second-leading cause of cancer death among men in the United States [1]. A transrectal ultrasound-guided biopsy is the clinical standard for diagnostic confirmation of suspected cancer. However, prostate lesions are often indistinguishable from surrounding healthy tissue in conventional B-mode ultrasound images [2], [3]. As a result, the procedure cannot be targeted to cancer-suspicious regions in the prostate, leading to a high rate of missed cancer upon initial biopsy and a need for repeat biopsies [4].

Acoustic radiation force impulse (ARFI) imaging has previously been shown to reliably identify clinically significant prostate lesions [5]. ARFI measures the displacement magnitude within the region of an acoustic radiation force push excitation to provide qualitative tissue elasticity information, with stiff tissues having lower displacements in response to the same force compared to softer tissues. On the other hand, shear wave elasticity imaging (SWEI) tracks the off-axis propagation of shear waves induced by the push beam to provide a quantitative shear wave speed (SWS) that is related to the underlying shear modulus of the tissue. In SWEI, higher shear wave speeds correspond to stiffer tissues.

A combined ARFI/SWEI sequence can obtain data for both modes simultaneously by transmitting a series of push beams across the lateral field of view and tracking both on- and off-axis after each push. In this study, we investigate the effect of the lateral push beam spacing on the quality of the reconstructed SWEI image using a combined ARFI/SWEI sequence in an elasticity lesion phantom. The shear wave tracking algorithm is implemented in human *in vivo* prostate data, and the matched SWEI and ARFI prostate images are compared with regards to visualization of prostate cancer and zonal anatomy.

## II. Methods

### A. Phantom Data Acquisition

Phantom data were acquired on the Verasonics ultrasound scanner (Verasonics, Inc., Redmond, WA) using the Philips L7-4 linear array transducer. A rapid three-focal-zone acoustic radiation force excitation with focal depths at 37.5 mm, 30 mm, and 22.5 mm was used to create a virtual, extended excitation through depth [6], [7]. At each focal depth, 400 cycles were transmitted using a frequency of 4 MHz and an F/3.5 focal configuration. Across the lateral field of view, 108 separate push excitations were used, spaced 0.3 mm apart. After each excitation, raw in-phase and quadrature (IQ) data were obtained at a 5-kHz pulse repetition frequency for 18 ms. A plane wave transmit, compounded with three steering angles at –3, 0, and 3 degrees, was used for tracking.

The phantom imaging target was a custom CIRS elasticity phantom (Norfolk, VA) that contained a stiff 5-mm diameter spherical inclusion in a background with a Young's modulus of 6.3 kPa. The impact of push beam density was examined by progressively downsampling the high-density push beam data and comparing the contrast-to-noise ratio (CNR) of the target in the reconstructed shear wave speed map. Data were separately acquired at two push excitation voltages, 50 V and 30 V, to explore the relation between shear wave amplitude, push beam spacing, and CNR. CNR was computed as $\frac{\mu_{in}-\mu_{out}}{\sqrt{\sigma_{in}^2+\sigma_{out}^2}}$, where $\mu_{in}$ and $\mu_{out}$ are the mean SWS values in the target and background, respectively, and $\sigma_{in}$ and $\sigma_{out}$ are the standard deviations of the values in each region.

### B. In Vivo Data Acquisition

In an ongoing, institutional review board-approved study with 36 subjects to date, combined ARFI/SWEI data has been obtained preoperatively in men expecting radical prostatectomy. Whole-mount histopathology data of the radically excised prostate were available for all imaged subjects. Data

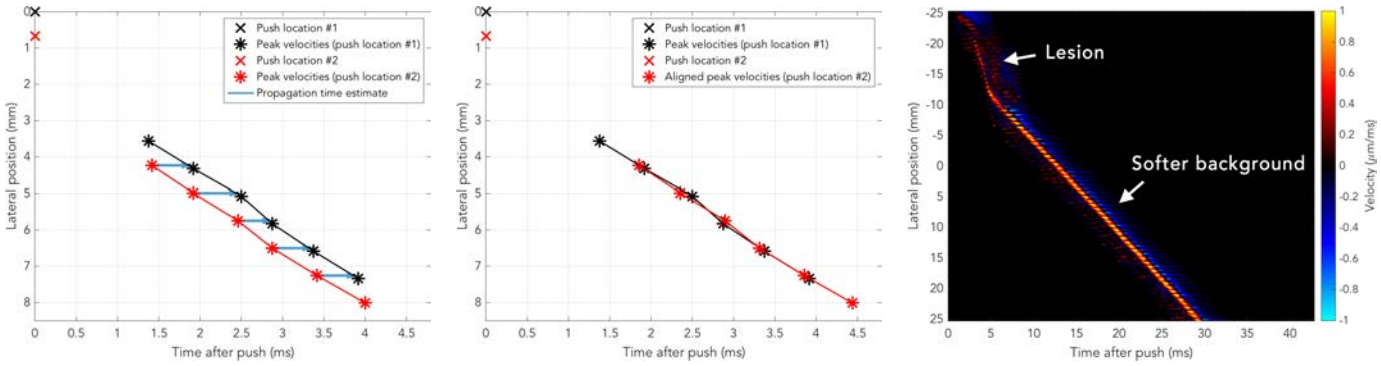


(a) (b) (c)

Fig. 1: (a) Estimation of shear wave propagation time between consecutive pushes. (b) Velocity signals aligned by temporally offsetting the second set of tracks by the estimated propagation time. (c) Aligned shear wave space-time trajectory over the entire field of view for a phantom with a 10-mm diameter stiff lesion.

were acquired using a Siemens SC2000 scanner (Siemens Medical Solutions USA, Inc., Issaquah, WA) with either an Acuson ER7B or Siemens 12L4 linear side-fire transrectal probe. The radiation force excitations again used three focal depths for an extended depth of field; the focal depths were at 30 mm, 22.5 mm, and 15 mm to accommodate the size of a typical prostate. Raw IQ data were obtained using tracking beams with 16:1 parallel receive [8]. The four center track beams were dedicated to tracking the on-axis ARFI displacement. Six track beams on either side of the excitation were used to track the left- and right-propagating shear waves, with 0.76-mm track beam spacing on each side. Eighty-two push beams, spaced 0.67 mm apart, were transmitted across the lateral field of view.

Three-dimensional prostate volumes were created by securing the transducer to a custom rotation stage and mechanically rotating it in approximately 1 degree increments between 2-D image acquisitions. First, matched ARFI and SWEI volumes were simultaneously obtained, and then the transducer was rotated back along the same trajectory to acquire high-resolution B-mode data.

### C. Shear Wave Tracking Algorithm

To estimate velocity through time from the beamformed IQ data, Loupas's 2D autocorrelation algorithm was applied to consecutive time steps [9], [10]. A low-pass filter with a cutoff frequency of 1.5 kHz was used to reduce jitter noise.

Directional filtering of the data was performed in three dimensions $(k_x, k_z, \omega)$ to reduce artifacts from reflections at stiff interfaces [11], [12]. In addition to separating rightward- from leftward-traveling shear waves, the 3-D directional filter attenuates spatial frequencies that are not primarily related to the $+x$ or $-x$ propagation direction (i.e., shear waves traveling obliquely to the push). The velocity signals were upsampled by a factor of three using spline interpolation to achieve more precise estimation of the shear wave arrival times.

The wave arrival times were determined using cross-correlation of the velocity signals in both the lateral and axial dimensions [13]. There were only six track lines on either side of the push in the *in vivo* sequence, resulting in few signals to cross-correlate. Therefore, to combine data from serially interrogated lateral push locations and obtain more robust estimates, this method was extended to include alignment of arrival times from different pushes, as described below.

Cross-correlation of velocity signals from consecutive pushes was used with linear interpolation to estimate the time it took for the shear wave to propagate between push locations. This is demonstrated in Fig. 1 (a), where the velocity signals are represented by their time to peak velocity values and the average of the blue arrows represent the estimated propagation time. Each of the velocity signals were temporally offset by the estimated propagation time, as shown in Fig. 1 (b), where the apparent spatial observation window has been increased by aligning the arrival times. Extending this method to the entire lateral field of view results in the space-time trajectory shown in Fig. 1 (c), where the spatial window over which the shear wave propagation is observed has been greatly increased.

Once aligned, estimates of shear wave speed were obtained by cross-correlation in two dimensions, including cross-correlation of aligned signals from different pushes. Estimates that were deemed low-quality were discarded if the correlation coefficient was low (under 0.6 for the *in vivo* prostate data) or if the SWS was outside the range of appropriate estimates (i.e., negative speeds or speeds over 12 m/s). The remaining estimates were then resampled to a gridded 2-D shear wave speed map using an algorithm weighted by the correlation coefficient associated with each estimate and its distance to the regridded pixel.

## III. Results and Discussion

### A. Impact of Push Beam Spacing

Phantom SWEI images with progressively downsampled push beam data are shown in Fig. 2 with means and standard deviations of shear wave speed values from the target and background. Pixels colored blue in the images represent NaN (not a number) values where there were no SWS estimates

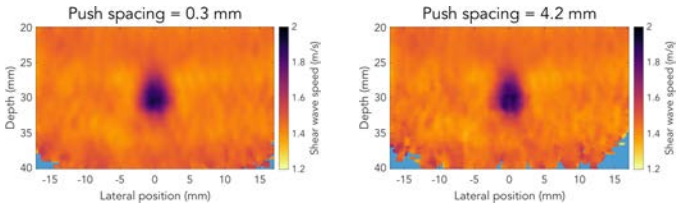


(a) Target: 1.84 ± 0.05 m/s, Background: 1.44 ± 0.01 m/s




(b) Target: 1.86 ± 0.07 m/s, Background: 1.44 ± 0.02 m/s

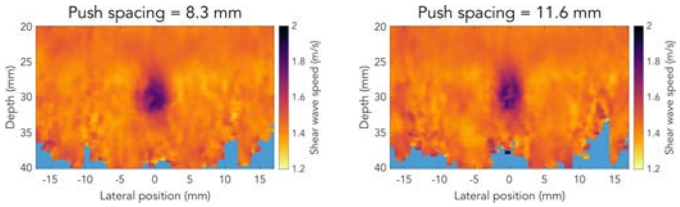


(c) Target: 1.82 ± 0.06 m/s, Background: 1.42 ± 0.03 m/s




(d) Target: 1.84 ± 0.11 m/s, Background: 1.46 ± 0.03 m/s

Fig. 2: Shear wave elasticity image reconstructions for down-sampled push beam data with push spacing of (a) 0.3 mm, (b) 4.2 mm, (c) 8.3 mm, and (d) 11.6 mm. Blue pixels indicate regions where the shear wave speed could not be estimated due to decorrelation.

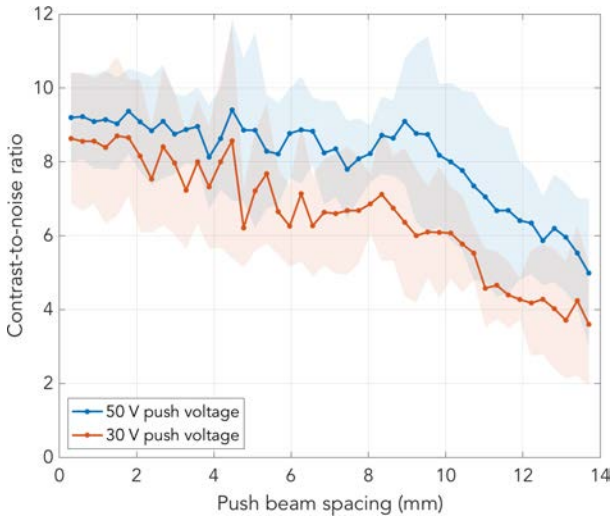


Fig. 3: Effects of push beam spacing and push excitation voltage on target contrast-to-noise ratio in the phantom dataset. Shaded error bars represent the standard deviation over six speckle realizations.

available for reconstruction after applying the correlation coefficient and shear wave speed thresholds. These images were reconstructed using 3-D directional filtering, which was found to improve the contrast-to-noise ratio compared to no directional filtering, independent of push beam spacing. A decrease in image quality can be observed with lower push beam density, with a higher degree of image artifacts, NaN pixels, and variablity in shear wave speed estimates appearing in the images with greater push spacing.

The downward trend of the two curves in Fig. 3 shows the decrease in CNR as the push beam data is increasingly down-sampled. Here, the shaded error bars represent the standard deviation over six independent speckle realizations. Increased variability of shear wave estimates with reduced push beam density contributes to the observed decrease in CNR. The difference between the blue and orange curves shows the impact of using different push excitation voltages. A lower voltage of 30 V, which resulted in lower particle displacements and therefore more noisy estimates, increased susceptibility to variable shear wave speed estimates and resulted in decreased CNR as shown in the plot.

To quantify the decrease in CNR, a linear regression was performed for each of the curves in Fig. 3. The slope of the linear fit for the 50 V push voltage data was –0.24 $\text{mm}^{-1}$, with an $R^2$ value of 0.72. For the 30 V push voltage data, the slope of the linear fit was –0.36 $\text{mm}^{-1}$, with an $R^2$ value of 0.89.

### *B. In Vivo Prostate SWEI*

Matched B-mode, SWEI, and ARFI images from an *in vivo* subject are shown in Fig. 4. These images display an axial view of the prostate, with the transducer located at the bottom of each image and rotated to produce the sector shape. The SWEI and ARFI data are the color regions displayed inside the segmented mask of the prostate capsule; B-mode data is displayed outside of the capsule for structural context. The ARFI color scheme was constructed from the histogram-normalized displacement magnitudes, where darker pixels correspond to lower displacements and thus higher stiffness. Similarly, darker regions in the SWEI images indicate higher shear wave speeds, which correspond to higher stiffness.

In Figs. 4 (b) and 4 (c), the white arrows in the SWEI and ARFI images indicate a region that appears stiff with contralateral contrast in both SWEI and ARFI. Since the prostate is typically symmetric in the axial view, the asymmetric stiff region is highly indicative of a prostate lesion. Indeed, this region was confirmed to be Gleason 6 prostate cancer in whole-mount histology. Furthermore, the stiff crescent-shaped central zone of the prostate can be distinguished from the softer surrounding peripheral zone in the center of the SWEI and ARFI images, with greater contrast compared to the corresponding B-mode image.

Fig. 5 shows matched B-mode, SWEI, and ARFI images from another *in vivo* case; this subject had histologically-confirmed Gleason 7 cancer, with a large lesion appearing stiff in both SWEI and ARFI with contralateral contrast. Once again, the SWEI image is concordant with ARFI, and the stiff central zone can be distinguished from the softer peripheral zone in these images. The urethra is also visible in the middle of the central gland as a structure that appears soft in both SWEI and ARFI.

## IV. Conclusions

We have implemented a new SWEI algorithm for a combined ARFI/SWEI prostate sequence that allows visualization

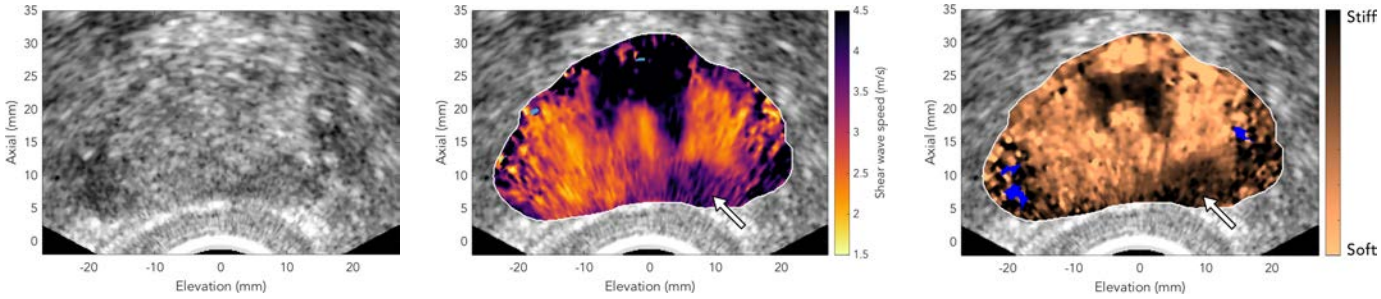


(a) Axial B-mode image. (b) Axial SWEI image. (c) Axial ARFI image.

Fig. 4: Matched B-mode, SWEI, and ARFI axial views of a Gleason 6 prostate lesion (arrow), confirmed in whole-mount histology.

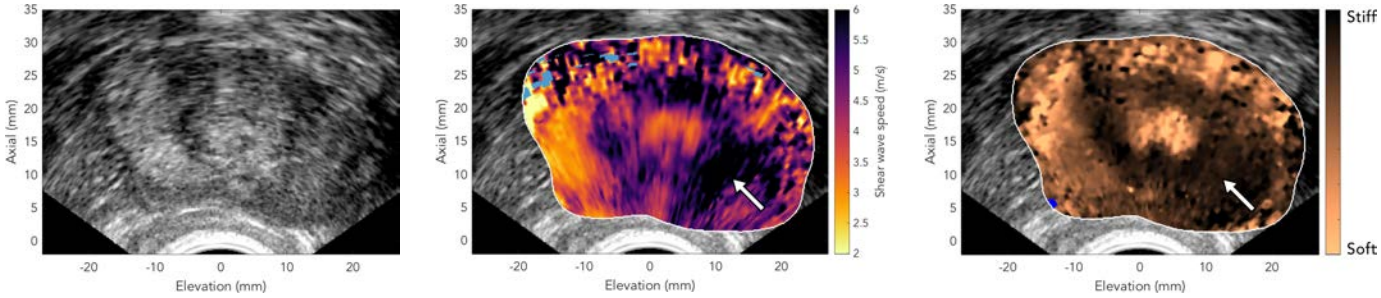


(a) Axial B-mode image. (b) Axial SWEI image. (c) Axial ARFI image.

Fig. 5: Matched B-mode, SWEI, and ARFI axial views of a large, histologically confirmed Gleason 7 prostate lesion (arrow).

of prostate cancer and zonal anatomy that is concordant with ARFI imaging. The combined sequence includes closely-spaced push beams for enhanced quality of the reconstructed shear wave speed images. Cancerous lesions appear stiff in both SWEI and ARFI, and the peripheral zone, central gland, and urethra display stiffness contrast as well. Using these elasticity image volumes will help provide imaging guidance for patients receiving a targeted prostate biopsy in a single clinic visit. Future work will explore sequence optimization based on tradeoffs between push beam density, frame rate, and transducer surface heating.

## Acknowledgments

This work was supported by NIH grants R01-CA142824 and T32-EB001040 and DOD PRCP grant W81XWH-16-1-0653. The authors are grateful to Siemens Medical Solutions USA, Ultrasound Division for in-kind and technical support. Special thanks to Stephen Rosenzweig and Annette Caenen for experimental support, and Ned Danieley for computer system administration.

## References

[1] R. L. Siegel, K. D. Miller, and A. Jemal, "Cancer statistics, 2018," CA Cancer J. Clin., vol. 68, no. 1, pp. 7–30, Jan. 2018.

[2] J. Raja, N. Ramachandran, G. Munneke, and U. Patel, "Current status of transrectal ultrasound-guided prostate biopsy in the diagnosis of prostate cancer," Clin. Radiol., vol. 61, no. 2, pp. 142–153, Feb. 2006.

[3] G. Salomon et al., "Evaluation of prostate cancer detection with ultrasound real-time elastography: a comparison with step section pathological analysis after radical prostatectomy," Eur. Radiol., vol. 54, no. 6, pp. 1354–1362, Dec. 2008.

[4] N. E. Abraham, N. Mendhiratta, and S. S. Taneja, "Patterns of repeat prostate biopsy in contemporary clinical practice," J. Urol., vol. 193, no. 4, pp. 1178–1184, April 2015.

[5] M. L. Palmeri et al., "Identifying clinically significant prostate cancers using 3-D in vivo acoustic radiation force impulse imaging with whole-mount histology validation," Ultrasound Med. Biol., vol. 42, no. 6, pp. 1251–1262, June 2016.

[6] J. Bercoff, M. Tanter, and M. Fink, "Supersonic shear imaging: a new technique for soft tissue elasticity mapping," IEEE Trans. Ultrason. Ferroelectr. Freq. Control, vol. 51, no. 4, pp. 396–409, April 2004.

[7] S. Rosenzweig, M. Palmeri, and K. Nightingale, "Analysis of rapid multi-focal zone ARFI imaging," IEEE Trans. Ultrason. Ferroelectr. Freq. Control, vol. 62, no. 2, pp. 280–289, Feb. 2015.

[8] J. Dahl et al., "A parallel tracking method for acoustic radiation force impulse imaging," IEEE Trans. Ultrason. Ferroelectr. Freq. Control, vol. 54, no. 2, pp. 301–312, Feb. 2007.

[9] T. Loupas, J. T. Powers, and R. W. Gill, "An axial velocity estimator for ultrasound blood flow imaging, based on a full evaluation of the Doppler equation by means of a two-dimensional autocorrelation approach," IEEE Trans. Ultrason. Ferroelectr. Freq. Control, vol. 42, no. 4, pp. 672–688, July 1995.

[10] G. F. Pinton, J. J. Dahl, and G. E. Trahey, "Rapid tracking of small displacements with ultrasound," IEEE Trans. Ultrason. Ferroelectr. Freq. Control, vol. 53, no. 6, pp. 1103–1117, June 2006.

[11] S. L. Lipman, N. C. Rouze, M. L. Palmeri, and K. R. Nightingale, "Evaluating the improvement in shear wave speed image quality using multidimensional directional filters in the presence of reflection artifacts," IEEE Trans. Ultrason. Ferroelectr. Freq. Control, vol. 63, no. 8, pp. 1049–1063, Aug. 2016.

[12] A. Manduca, D. S. Lake, S. A. Kruse, and R. L. Ehman, "Spatio-temporal directional filtering for improved inversion of MR elastography images," Med. Image Anal., vol. 7, no. 4, pp. 465–473, Dec. 2003.

[13] P. Song et al., "Fast shear compounding using robust 2-D shear wave speed calculation and multidirectional filtering,", Ultrasound Med. Biol., vol. 40, no. 6, pp. 1343–1355, June 2014.

# Correlation between 3D ARFI and quantitative imaging metrics from SWEI and multi-parametric MRI *in vivo* in normal and cancerous prostate tissue

D. Cody Morris*, Derek Y. Chan*, Mark L. Palmeri*, Tyler J. Glass*, Matthew M. McCormick†,
K. Jack Tay‡, Thomas J. Polascik‡, Rajan T. Gupta‡, Kathryn R. Nightingale*
*Department of Biomedical Engineering, Duke University, Durham, NC, USA,
† Medical Computing Group, Kitware Inc., Clifton Park, NY, USA,
‡ Duke University Medical Center, Durham, NC, USA
Email: cody.morris@duke.edu

***Abstract*—Prostate lesions and healthy regions from 12 radical prostatectomy patients were identified in acoustic radiation force impulse (ARFI) imaging, shear wave elasticity imaging (SWEI), and multi-parametric magnetic resonance imaging (mpMRI) apparent diffusion coefficient (ADC) data and confirmed by histopathology. Custom sequencing and processing techniques led to ARFI and SWEI images which demonstrate strong structural concordance. The combination of quantitative metrics from multiple imaging modalities using a principal component binary discriminator improved the diagnostic capability over individual modalities with areas under the receiver operating characteristic curve reaching 0.94. The correlations among the separate modality parameters were moderate with R-squared values between 0.47 (ADC and ARFI) and 0.71 (ARFI and SWEI).**

## I. Introduction & Background

Prostate cancer (PCa) is diagnosed in approximately 1 in 9 American men [1]. The gold standard for diagnosing PCa is transrectal ultrasound (TRUS) guided biopsy which consists of 10-12 systematically sampled cores taken throughout the prostate [2]. Due to the sensitivity and specificity limitations of standard TRUS biopsy [3], 3-D imaging methods with increased PCa contrast, such as multiparametric magnetic resonance imaging (mpMRI), can be used in an image fusion approach for lesion targeting [4]. Acoustic radiation force impulse (ARFI) imaging and shear wave elasticity imaging (SWEI) are two elasticity imaging methods which are being actively explored as supplements to mpMRI as they have potential to be real time and readily accessible [5][6][7][8].

ARFI imaging utilizes focused acoustic radiation force push excitations to induce micron level displacements in tissue. These displacements are ultrasonically tracked through time at the location of excitation and images of relative stiffness across the field of view from multiple sequential pushes are created [9]. SWEI uses the same push beams but tracks the displacements through time at positions laterally offset to capture shear wave propagation [10]. This propagation is used to generate a quantitative image of the stiffness across the imaging window. Both ARFI and SWEI methods are sensitive to PCa and identify it as stiffer than the surrounding healthy tissue [5][6][7][8].

Recent work has suggested that ARFI imaging and mpMRI could be combined to improve diagnostic capability [6]. In this work, quantitative metrics from ARFI, SWEI, and the apparent diffusion coefficient (ADC) value from mpMRI, which has been added to the Prostate Imaging - Reporting and Data System version 2 (PI-RADSv2) as a suggested threshold metric to separate benign from malignant tissue [11], will be measured *in vivo* in cancerous and healthy prostate tissue. Both the correlation among these parameters and the area under the receiver operator characteristic curve (AUROC), which is assessed for each individual metric and their combinations, are examined for added diagnostic value. This work is a step toward achieving real-time ultrasound targeting for prostate biopsy.

## II. Methods

### A. Prostate Volume Acquisition

Ultrasonic data was acquired in 12 patients immediately preceding a radical prostatectomy for PCa using a modified Siemens SC2000 (Siemens Medical Solutions, Mountain View, CA) and an Acuson ER7B or custom 12L4 ultrasound probe paired with a rotation stage to acquire sagittal images of the prostate with a 1-1.5° angular spacing. These images were scan converted into a 3D volume using 3D Slicer (Kitware Inc., Clifton Park, NY) [12]. ARFI and SWEI data was acquired simultaneously and thus these volumes are co-registered (Figure 1). A detailed overview of the ultrasonic acquisition can be found in [6]. A preoperative mpMRI was also performed in each patient using a 3T endorectal coil system to generate the ADC volume. Each prostate underwent whole mount histology post radical prostatectomy to provide ground truth identification of the lesions visible in the three imaging modalities. All data were acquired under an institutional review board-approved study after obtaining written informed consent.

### B. ARFI and SWEI Processing

For both the ARFI and SWEI volumes, displacement estimation was performed using the Loupas phase shift estimator [13]. A correlation coefficient mask with a threshold of 0.95 was applied to the data to limit the impact of noise.

Further ARFI processing was performed as previously described [6][7]. The data identified as prostate tissue by semi-automated segmentation in 3D Slicer [12] was then histogram equalized to enhance the image contrast.

The SWEI data was processed using methods described by Manduca *et al.* [14], Lipman *et al.* [15], and Song *et al.* [16]. The velocity waveform data was first low pass filtered with a cutoff frequency of 1.5 kHz. Then the data was 3D directionally filtered [14][15]. Shear wave speeds were estimated using 2D vector tracking [16], discarding speed estimates greater than 12m/s or with correlation coefficients $< 0.6$.

### C. Target Identification

The index lesion was identified and conservatively segmented using 3D Slicer for both ARFI and ADC volumes based on cognitive fusion with histologically determined ground truth [12]. The ARFI segmentation was extended to the SWEI volume and adjusted based on the SWEI lesion contrast to identify a concordant suspicious region in both modalities. The segmentations were left-right mirrored to identify healthy tissue in the contralateral hemisphere (Figure 2). In one case where the contralateral side also corresponded to disease, healthy tissue was identified separately.

### D. Parameter Combination

To assess the benefit of combining modalities, the AUROC was calculated for each parameter. The three modality parameters were normalized to values between 0 and 1 and their correlation was examined. This normalized data was also used with a principle component based binary discriminator which combines the values from the individual parameters into a single parameter. The AUROC was then calculated for the discriminators and compared to the unpaired datasets. This analysis was also extended to 3D to combine all three parameters. Due to the low resolution and lack of co-registration, analyses including ADC are limited to medians of the voxel distribution resulting in coarse receiver operating characteristic (ROC) curves and non-representative AUROCs.

## III. Results & Discussion

Sample images of the ARFI and SWEI volumes are shown in Figure 1. These modalities demonstrate structural concordance which facilitates performing voxel based analysis. Figure 2 further demonstrates the ARFI/SWEI concordance along with approximate alignment to the corresponding mpMRI ADC images. In Figure 2, the segmentations used to determine parameter distributions are included which indicate lesion (yellow outline) and healthy (green outline) tissue.

Figure 3 portrays the thresholds with the distribution of voxels in each segmentation included as boxplots. Thresholds are determined with the medians of the voxels in each segmentation (Figure 3 A) or using the entire distribution of voxels (Figure 3 B and C). An ADC threshold of 1160 (Figure 3 A) separates PCa from healthy tissue with one false positive. The empirically determined ADC threshold is different from the clinically established PI-RADSv2 threshold (750-900) which results in five false negatives in our data. ARFI and SWEI thresholds (Figure 3 B and C) are a pixel intensity of 93.5 with an AUROC of 0.92 and a shear wave speed of 4.60 m/s with an AUROC of 0.87, respectively. This suggests that even before the combination of metrics, ARFI and SWEI out perform the PI-RADSv2 ADC threshold.

TABLE I
Analysis of individual parameters and their combinations

| Combination | AUROC | Threshold | PC vector | $R^2$ |
|---|---|---|---|---|
| ADC | | 1159.5 | | |
| ARFI | 0.92 | 93.5 | | |
| SWEI | 0.87 | 4.60 | | |
| ADC, ARFI | | 0.65 | <0.66, 0.75> | 0.47 |
| ADC, SWEI | | 0.23 | <-0.70, 0.71> | 0.51 |
| ARFI, SWEI | 0.94 | 0.17 | <0.84, -.54> | 0.71 |
| ADC, ARFI, SWEI | | 0.34 | <0.53, 0.62, -0.58> | |

Figure 3 D shows the distribution and threshold between healthy and lesion for the combination of ARFI and SWEI. The normalized parameter is a unitless combination defined by the principal component analysis (in MATLAB). Figure 4 C demonstrates the combination of ARFI and SWEI with the appropriate threshold. The AUROC for the combination of ARFI and SWEI is 0.93 and the ROC curve is shown in Figure 4 D. Figure 4 A and B show the combination of ARFI and ADC, and SWEI and ADC, respectively. The ARFI and SWEI combinations with ADC achieve perfect separation. In Figure 4 A, B and C, the lesion medians are indicated in red, healthy tissue medians are in blue, and the threshold by the magenta line. The combination of all three parameters also results in perfect separation. The increased AUROC for the combination of ARFI and SWEI, and the perfect separation when combining either or both parameters with ADC, is indicative of a benefit provided to diagnostic capability by including information from multiple modalities. This benefit is particularly apparent in the case of patient 12, which is a false positive by ADC but is correctly identified as negative when combined with ARFI/SWEI.

The individual and parameter combination results are summarized in Table I. Also included in Table I are the principal component vectors used with the binary discriminator and the R-squared values for the paired combinations. The principal component vectors indicate the weight which is applied to the individual parameters in the combination. As all values are non-zero, combining modalities provides additional information for the discrimination of lesions from healthy tissue. The R-squared values calculated for the combination of two parameters are particularly low, which indicates that there is information to be gained by combining modalities.

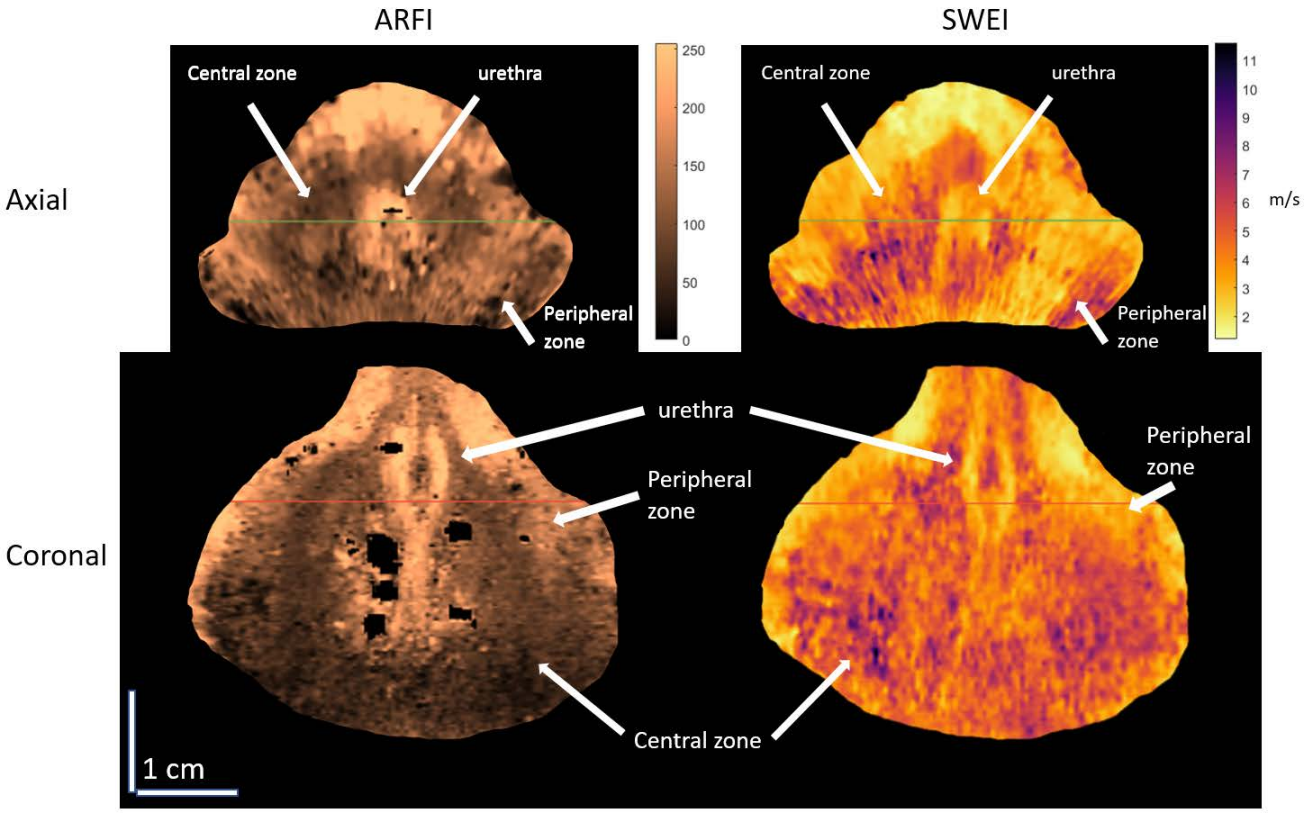


Fig. 1. Sample ARFI (left) and SWEI (right) registered images demonstrating structural concordance. Axial (top) and coronal (bottom) images both demonstrate symmetry and allow for delineation of the prostate capsule.

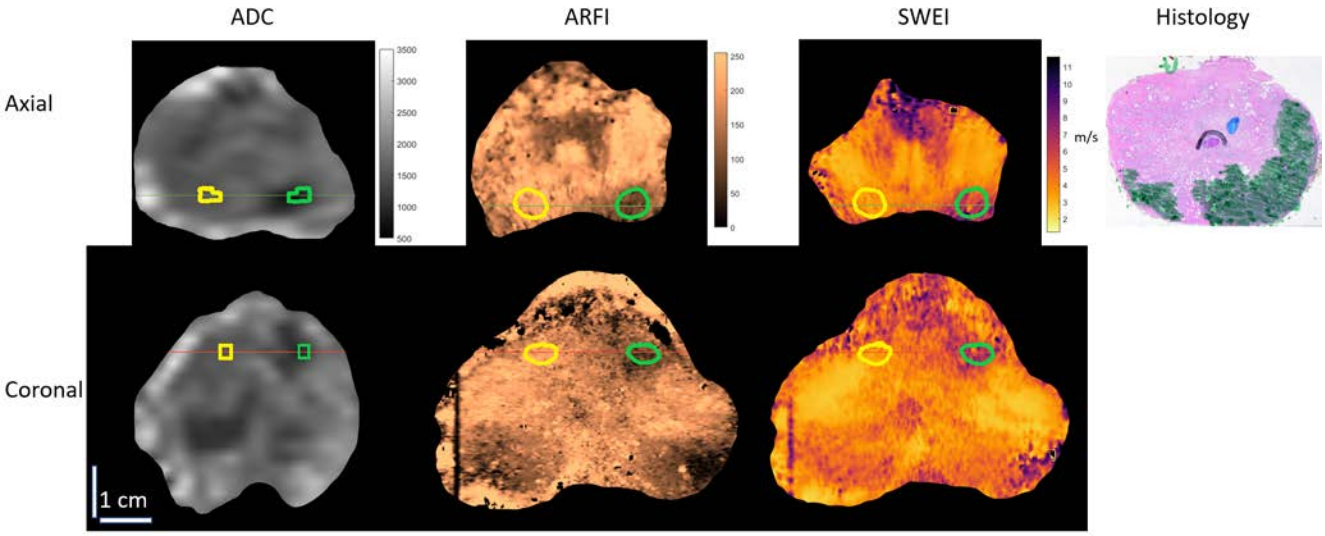


Fig. 2. Sample mpMRI ADC (left), ARFI (middle-left), SWEI (middle-right), and histology (right) images demonstrating the lesion and healthy region identification process. ARFI and SWEI images are perfectly registered with cognitive registration performed on ADC and histology. In all images the lesion is identified (yellow outline) and this segmentation is mirrored to the contralateral side to identify a healthy region (green outline). Segmented regions are shown in axial (top) and coronal (bottom) imaging planes. Histology shows Gleason 3+3 in green.

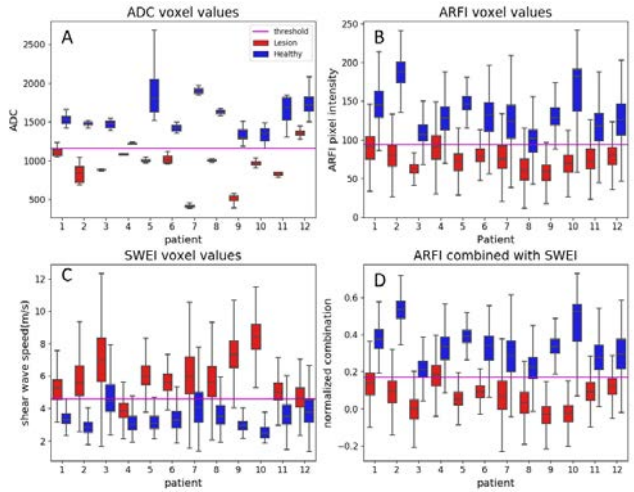


Fig. 3. The distribution of values within each segmentation for ADC (A), ARFI (B), SWEI (C), and the combination of ARFI and SWEI (D). Thresholds are included which are defined by ROC analysis of the entire distribution (B,C,D). AUROCs are included in Table I. The threshold included in subplot A is defined by ROC analysis of the medians, identifying one false positive based on mpMRI alone.

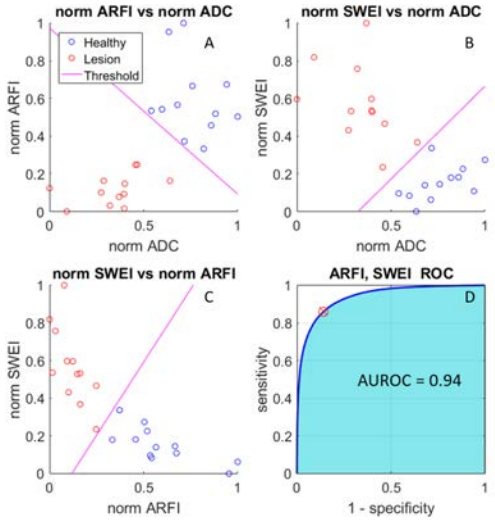


Fig. 4. Subplots A, B, and C, demonstrate the correlation between ARFI and ADC, SWEI and ADC, and SWEI and ARFI, respectively. Subplot C is the combination of ARFI and SWEI voxels with the corresponding ROC curve in subplot D. Medians of the distributions are used for visualization where healthy tissue is blue and lesions are red. Thresholds determined by the binary discriminator are represented by the magenta lines.

## IV. Limitations

PCa was identifed in ARFI and mpMRI based on their locations as specified in histopathology following radical prostatectomy. This limits the patients recruited to those with confirmed significant disease. Also as the ARFI segmentations were extended to SWEI, only the overlapping volumes were used. This limits the lesion data analyzed to regions classified as suspicious in all three imaging modalities, and excluded cases where PCa was only indicated in a subset, which may inflate the AUROCs and bias the discrimination thresholds.

## V. Conclusion

Custom ARFI and SWEI sequencing and processing techniques lead to prostate images with structural concordance. The combination of quantitative metrics from ARFI, SWEI and mpMRI ADC improves the diagnostic capability of the individual modality metrics with AUROCs reaching 0.94. The correlations among the modality parameters are moderate with R-squared values between 0.47 (ADC and ARFI) and 0.71 (ARFI and SWEI).

## Acknowledgements

This work was supported by National Institutes of Health (NIH) Grants R01 CA142824 and T32-EB001040 and Department of Defense (DoD) Grant USAMRMC award number W81XWH-16-1-0653. The authors thank Siemens Medical Solutions USA, Ultrasound Division, for their in-kind technical support.

## References

[1] R. L. Siegel, K. D. Miller, and A. Jemal, Cancer statistics, 2018, *CA. Cancer J. Clin.*, vol. 68, no. 1, pp. 730, 2018.

[2] N. Mottet *et al.*, EAU-ESTRO-SIOG Guidelines on Prostate Cancer. Part 1: Screening, Diagnosis, and Local Treatment with Curative Intent, *Eur. Urol.*, vol. 71, no. 4, pp. 618 629, 2017.

[3] J. Correas, A. Tissier, and A. Khairoune, Ultrasound elastography of the prostate: State of the art, *Diagn. Interv. Imaging*, vol. 94, no. 5, pp. 551560, 2013.

[4] M. M. Siddiqui *et al.*, Comparison of MR/ultrasound fusion-guided biopsy with ultrasound-guided biopsy for the diagnosis of prostate cancer, *JAMA - J. Am. Med. Assoc.*, vol. 313, no. 4, pp. 390397, 2015.

[5] R. G. Barr, R. Memo, and C. R. Schaub, Shear wave ultrasound elastography of the prostate: Initial results, *Ultrasound Q.*, vol. 28, no. 1, pp. 1320, 2012.

[6] M. L. Palmeri *et al.*, Identifying Clinically Significant Prostate Cancers using 3-D *In Vivo* Acoustic Radiation Force Impulse Imaging with Whole-Mount Histology Validation, *Ultrasound Med. Biol.*, vol. 42, no. 6, pp. 12511262, 2016.

[7] S. Rosenzweig *et al.*, Comparison of concurrently acquired in vivo 3D ARFI and SWEI images of the prostate, *IEEE Int. Ultrason. Symp. IUS*, pp. 97100, 2012.

[8] O. Rouvire *et al.*, Stiffness of benign and malignant prostate tissue measured by shearwave elastography: a preliminary study, *Eur. Radiol.*, vol. 27, no. 5, pp. 18581866, 2017.

[9] K. Nightingale *et al.*, "Acoustic Radiation Force Impulse Imaging: *in vivo* Demonstration of Clinincal Feasiblity," *Ultrasound Med. Biol.*, vol. 28, no. 2, pp. 227-235, 2002.

[10] A. Sarvazyan *et al.*, "Shear Wave Elasticity Imaging: A New Ultrasonic Technology of Medical Diagnostics," *Ultrasound Med. Biol.*, vol. 24, no. 9, pp. 1419-1435, 1998.

[11] P. Steiger, H. Thoeny, "Prostate MRI based on PI=RADS version 2: how we review and report," *Cancer Imaging*, vol. 6, no. 9, 2016.

[12] A. Fedorov *et al.*, 3D Slicer as an image computing platform for the Quantitative Imaging Network, *Magn. Reson. Imaging*, vol. 30, no. 9, pp. 13231341, 2012.

[13] T. Loupas, R. Peterson, R. Gill, Experimental evaluation of velocity and power estimation for ultrasound blood flow imaging, by means of a two-dimensional autocorrelation approach, *IEEE Trans Ultrason Ferroelectr Freq Control* vol. 42 pp. 689699, 1995.

[14] A. Manduca, *et al.*, "Spatiotemporal directional filtering for improved inversion of MR elastography images," /emphMed. Image Anal., vol. 7, no. 4, pp. 4650473, 2003.

[15] S. Lipman, *et al.*, "Evaluating the Improvement in Shear Wave Speed Image Quality Using Multidimensional Directional Filters in the Presence of Reflection Artifacts," /emphIEEE Trans Ultrason Ferroelectr Freq Control vol. 63, No. 8, pp. 1049-1063, 2016.

[16] P. Song, *et al.*, "Fast Shear Compounding using Robust 2-D Shear Wave Speed Calculation and Multi-Directional Filtering," *Ultrasound Med. Biol.*, vol. 40, no. 6, pp. 1343-1355, 2014.